Enhancement of the Krylov Subspace Regularization for Microwave Biomedical Imaging

Puyan Mojabi* and Joe LoVetri, *Senior Member, IEEE*

Abstract—Although Krylov subspace methods provide fast regularization techniques for the microwave imaging problem, they cannot preserve the edges of the object being imaged and may result in an oscillatory reconstruction. To suppress these spurious oscillations and to provide an edge-preserving regularization, we use a multiplicative regularizer which improves the reconstruction results significantly while adding little computational complexity to the inversion algorithm. We show the inversion results for a real human forearm assuming the 2-D transverse magnetic illumination and a cylindrical object assuming the 2-D transverse electric illumination.

Index Terms—Image reconstruction, microwave imaging.

I. INTRODUCTION

MICROWAVE imaging (MWI), as a biomedical imaging modality, uses microwave scattering measurements to quantitatively reconstruct the complex permittivity of the object of interest (OI), which is biological tissue *in situ*. Some current indications are that MWI can be useful for breast cancer imaging [1], [2], bone imaging [3], and the detection of ischemia in different parts of the body [4]. It is well known that the MWI problem is nonlinear and ill-posed. The nonlinearity of the problem may be addressed by employing appropriate optimization techniques such as the Gauss–Newton method [1], [5]–[8]. The ill-posedness is treated via regularization which may be achieved by enforcing the solution to lie in an appropriate subspace. The Krylov subspace techniques, e.g., conjugate gradient least squares (CGLS) method, iteratively project the solution onto Krylov subspaces of increasing dimension [9]. These iterative algorithms, when applied to an ill-posed system of equations, exhibit a *semi-convergence* behavior [10]. That is, they improve the solution at their early iterations, where the solution space is restricted to a Krylov subspace of small dimension. However, they start deteriorating the solution by inverting the noise in later iterations. An appropriately regularized solution can therefore be obtained by early termination of the utilized Krylov subspace algorithm when the dimension of the subspace is large enough to produce a good regularized solution and small enough to suppress the effect of noise. Therefore, the iter-

*P. Mojabi is with the Department of Electrical and Computer Engineering, University of Manitoba, Winnipeg, MB, R3T5V6, Canada (e-mail: pmojabi@ee.umanitoba.ca).

J. LoVetri is with the Department of Electrical and Computer Engineering, University of Manitoba, Winnipeg, MB, R3T5V6, Canada.

Color versions of one or more of the figures in this paper are available online at http://ieeexplore.ieee.org.

ation at which the algorithm is stopped plays the role of the regularization parameter for this type of regularization: the fewer the iterations, the stronger the regularization. Krylov subspace regularization methods provide very fast regularization techniques as 1) they are only based on a few matrix-vector multiplications and 2) they do not require the full storage of the ill-posed matrix. However, Krylov subspace regularization methods do not have the edge-preserving characteristic as defined in [11]. In addition, they may result in an oscillatory reconstruction when the signal to noise ratio of the measured data is not high enough.

Recently, the CGLS regularization technique, has been successfully used with the Gauss–Newton inversion (GNI) method for the microwave breast imaging application where a two-step procedure was used to determine the stopping iteration [1], [12]. Herein, we employ the CGLS regularization technique in the framework of the GNI method. We then use a multiplicative regularizer (MR) [13], in a post-regularization procedure, to suppress possible spurious oscillations associated with this Krylov subspace regularization and also to provide an edge-preserving regularization. While improving the results significantly, the utilized MR adds little computational complexity to the inversion algorithm. The regularization weight for the MR enhancement is determined automatically by the algorithm itself. We show the inversion results using this enhanced Krylov subspace regularization for transverse magnetic (TM) and transverse electric (TE) experimental data.

II. PROBLEM STATEMENT

Consider an imaging domain $\mathcal{D} \subset \mathbb{R}^2$, immersed in a known homogeneous background with relative permittivity ϵ_b, which contains a nonmagnetic OI with an unknown complex relative permittivity $\epsilon_r(\boldsymbol{q})$, $\boldsymbol{q} \in \mathcal{D}$. We assume that the Green's function for the background medium, $g(\boldsymbol{p}, \boldsymbol{q})$, is known. The electric contrast, defined as $\chi(\boldsymbol{q}) = (\epsilon_r(\boldsymbol{q}) - \epsilon_b)/\epsilon_b$, is to be found using the measured electric field data on a discrete measurement space $\mathcal{S} \subset \mathbb{R}^2$ outside $\mathcal{D}$. Denoting E^{meas} as the measured scattered field on $\mathcal{S}$ and E^{scat} as the simulated scattered field due to a predicted contrast χ, the MWI problem may then be formulated as the minimization over χ of the following nonlinear cost-functional:

$$\mathcal{F}^{\mathcal{LS}}(\chi) = \frac{1}{||E^{\text{meas}}(\boldsymbol{p})||^2_{\mathcal{S}}} ||E^{\text{scat}}(\boldsymbol{p}, \chi) - E^{\text{meas}}(\boldsymbol{p})||^2_{\mathcal{S}} \quad (1)$$

where $|| \cdot ||_{\mathcal{S}}$ denotes the L_2-norm on $\mathcal{S}$ and $\boldsymbol{p} \in \mathcal{S}$. Denoting the wavenumber of the background medium as k_b, and for simplicity of notation, assuming the 2-D TM formulation, the simulated scattered field on $\mathcal{S}$ due to the contrast χ can be written as

$$E^{\text{scat}}(\boldsymbol{p}, \chi) = k_b^2 \int_{\mathcal{D}} g(\boldsymbol{p}, \boldsymbol{q}) E(\boldsymbol{q}) \chi(\boldsymbol{q}) dv(\boldsymbol{q}) \quad (2)$$

where E represents the total field inside $\mathcal{D}$ which is a function of χ. To cope with the nonlinearity of the problem, we use the Gauss–Newton method to minimize (1); thus, the contrast at the nth stage of the algorithm is updated as $\chi_n = \chi_{n-1} + \nu_n \Delta\chi_n$ where $\Delta\chi_n$ and ν_n are the Gauss–Newton correction and an appropriate step-length, respectively. The step-length ν_n is a real positive number which is determined using a line search algorithm based on that described in [14] and [15]. The Gauss-Newton correction is found by solving

$$\boldsymbol{J}_{n-1}\Delta\chi_n = E^{\mathrm{meas}} - E^{\mathrm{scat}}_{n-1} \qquad (3)$$

where $\boldsymbol{J}_{n-1}$ denotes the Jacobian matrix containing the Fréchet derivative of $E^{\mathrm{scat}}(\boldsymbol{p}, \chi)$ with respect to χ evaluated at χ_{n-1}. The field E^{scat}_{n-1} represents the simulated scattered field at the observation points, $\boldsymbol{p} \in \mathcal{S}$, corresponding to the predicted contrast χ_{n-1}. Due to the ill-posedness of the cost-functional, the matrix $\boldsymbol{J}_{n-1}$ is severely ill-conditioned; thus, (3) needs to be regularized to give an acceptable $\Delta\chi_n$. Herein, we regularize (3) by iteratively projecting $\Delta\chi_n$ onto CGLS Krylov subspaces of increasing dimension and use the same two-step procedure as in [1] to determine the stopping iteration of the CGLS scheme. We will refer to this inversion algorithm as GNI-CGLS in this paper.

III. ENHANCEMENT OF THE RECONSTRUCTION

Inspired by the work of Abubakar *et al.* on an edge-preserving regularization technique [13], we enhance the final reconstruction of the GNI-CGLS method by the weighted L_2-norm total variation MR. Denoting the final reconstruction of the GNI-CGLS method as $\hat{\chi}$, we accomplish that by first approximating the nonlinear operator $E^{\mathrm{scat}}(\boldsymbol{p}, \chi)$, (2), with the linear operator $E^{\mathrm{scat}}_{\mathrm{Lin}}(\boldsymbol{p}, \chi)$ defined as

$$E^{\mathrm{scat}}_{\mathrm{Lin}}(\boldsymbol{p}, \chi) = k_b^2 \int_{\mathcal{D}} g(\boldsymbol{p}, \boldsymbol{q}) E^{\hat{\chi}}(\boldsymbol{q}) \chi(\boldsymbol{q}) dv(\boldsymbol{q}) \qquad (4)$$

where $E^{\hat{\chi}}(\boldsymbol{q})$ is the known total field inside $\mathcal{D}$ due to the known contrast $\hat{\chi}$. We then construct a multiplicatively regularized cost-functional as

$$\mathcal{C}(\chi) = \left\| E^{\mathrm{scat}}_{\mathrm{Lin}}(\boldsymbol{p}, \chi) - E^{\mathrm{meas}}(\boldsymbol{p}) \right\|_{\mathcal{S}}^2 \mathcal{F}^{\mathcal{MR}}(\chi). \qquad (5)$$

This multiplicatively regularized cost-functional is minimized using the CG method over the contrast χ where the initial guess to the CG algorithm is $\hat{\chi}$. Thus, the contrast is iteratively enhanced as $\chi_m = \chi_{m-1} + \alpha_m d_m$ where d_m is the CG direction at the mth iterate of the enhancement procedure and α_m is a real constant number. At the mth iteration of the CG method, the multiplicative regularizer is given by

$$\mathcal{F}_m^{\mathcal{MR}}(\chi) = \frac{1}{A} \int_{\mathcal{D}} \frac{|\nabla\chi(\boldsymbol{q})|^2 + \delta_m^2}{|\nabla\chi_{m-1}(\boldsymbol{q})|^2 + \delta_{m-1}^2} dv(\boldsymbol{q}) \qquad (6)$$

where A represents the area of $\mathcal{D}$ and ∇ denotes the spatial gradient operator with respect to the position vector $\boldsymbol{q}$. To ensure the convexity of the cost-functional (5), the positive parameter δ_m^2 is chosen to be [13]

$$\delta_m^2 = \frac{1}{2} \frac{\|b_m \nabla\chi_{m-1}\|_{\mathcal{D}}^2}{\|b_m\|_{\mathcal{D}}^2} \qquad (7)$$

where $b_m = A^{-1/2}(|\nabla\chi_{m-1}|^2 + \delta_{m-1}^2)^{-1/2}$ and $\|\cdot\|_{\mathcal{D}}$ denotes the L_2-norm on $\mathcal{D}$. As this MR can be represented as an L_2-norm functional, the CG direction d_m and the real parameter

α_m are available in closed form [13]. Therefore, the computational cost of this enhancement is almost negligible compared to that of the inversion algorithm. It should also be noted that if the GNI-CGLS method is partially converged, the MR enhancement will enhance the partially-converged reconstruction. This has been demonstrated in Section IV-A.

The gradient operator of $\mathcal{F}_m^{\mathcal{MR}}$, which is $-\nabla \cdot (b_m \nabla)$, has the same form as the gradient of the well-known edge-preserving L_1-norm total variation additive regularizer; thus, the MR can provide an edge-preserving regularization through its gradient [13]. The operator $-\nabla \cdot (b_m \nabla)$ provides a weighted Laplacian operator where the weight b_m controls the edge-preserving properties of this operator [11]. That is, if one specific region of χ_{m-1} is homogeneous, the weight b_m will be almost constant for that part and the operator $-\nabla \cdot (b_m \nabla)$, when applied to that region, will be approximately $-b_m \nabla^2$ which favors smooth solution (due to the presence of the Laplacian operator ∇^2). Thus, the smoothness will be preserved in that region. On the other hand, if there is a large gradient in χ_{m-1} (e.g., an edge in the image) in some part of $\mathcal{D}$, the corresponding b_m for that region will be small. Therefore, the steep gradient will not be smoothed out but will be preserved [11]. As opposed to edge-preserving regularization techniques presented in [16] and [17], the weighting function b_m and the regularization weight are determined automatically by the algorithm itself [13].

The enhancement procedure terminates when the normalized difference between two successive enhanced contrasts becomes less than a prescribed tolerance [13], i.e.,

$$\frac{\|\chi_m - \chi_{m-1}\|_{\mathcal{D}}^2}{\|\chi_m\|_{\mathcal{D}}^2} < \mathrm{tol.} \qquad (8)$$

In our implementation, the prescribed tolerance is set to be 10^{-6}.

It should be mentioned that $\mathcal{F}^{\mathcal{MR}}(\chi)$ can also be included as the multiplicative regularization term to the nonlinear data misfit cost-functional $\mathcal{F}^{\mathcal{LS}}(\chi)$ [14], [18]. The Gauss-Newton optimization can then be applied to this multiplicatively regularized nonlinear cost-functional $\mathcal{F}^{\mathcal{LS}}(\chi)\mathcal{F}^{\mathcal{MR}}(\chi)$ [14], [18]. The GNI-CGLS method in conjunction with the MR enhancement, utilized in this paper, is computationally more efficient than this technique. This is discussed in the Appendix.

IV. INVERSION RESULTS

We consider two targets from two different experimental data sets. The first target is a real human forearm assuming the 2-D TM illumination and the other one is a combination of two cylinders assuming the 2-D TE illumination. In both cases, we start the inversion algorithm with $\chi = 0$. The GNI-CGLS and the MR enhancement were run as Matlab scripts on quad-core 2.66-GHz machine. The utilized forward solver in the GNI method is a method of moments (MoM) solver which utilizes the CG method accelerated by the fast Fourier transform (FFT) [19] and the marching-on-in-source-position technique [20].

A. Real Human Forearm

The BRAGREG data set (data file: BRAGREG.ASC) is collected from a real human forearm by a near-field single-frequency (2.33 GHz) scanner by the Universitat Politècnica de Catalunya (UPC), Barcelona [21]. The background medium is
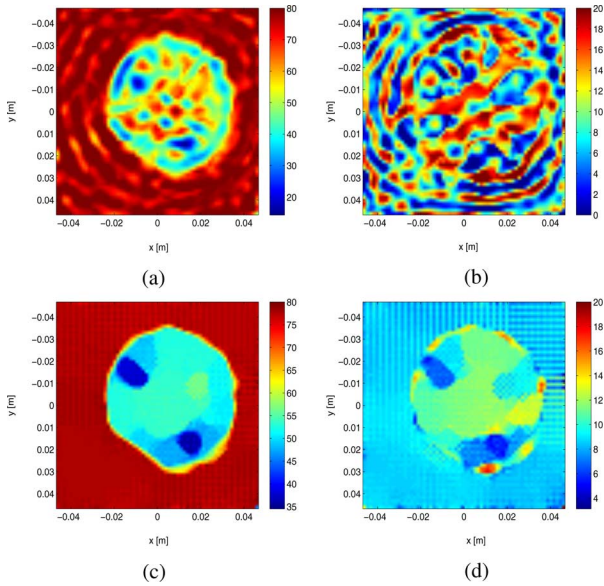
Fig. 1. Reconstruction of the real human forearm (a), (b) using the GNI-CGLS method and (c), (d) using the MR-enhanced GNI-CGLS method. (a) $\text{Real}(\epsilon_r)$, (b) $\text{Imag}(\epsilon_r)$, (c) $\text{Real}(\epsilon_r)$, and (d) $\text{Imag}(\epsilon_r)$.

Fig. 2. (a), (b) Reconstruction of the human forearm at the 5th iteration of the GNI-CGLS and (c), (d) its corresponding MR-enhanced reconstruction. (a) $\text{Real}(\epsilon_r)$, (b) $\text{Imag}(\epsilon_r)$, (c) $\text{Real}(\epsilon_r)$, and (d) $\text{Imag}(\epsilon_r)$.

water, with the relative permittivity of $\epsilon_b = 77.3 + j8.66$ at 2.33 GHz. There are 64 transmitting antenna and 33 active receivers for each transmitter. The measured data is then calibrated using an electric line source assuming the 2-D TM illumination [22]. In this case, we consider the imaging domain $\mathcal{D}$ to be a 9.36 cm × 9.36 cm square discretized into 64 × 64 pulse basis functions. The inversion results were restricted to lie within $0 \leq \text{Real}(\epsilon_r) \leq 80$ and $0 \leq \text{Imag}(\epsilon_r) \leq 20$ as in [22]. The expected relative permittivities at 2.33 GHz are approximately $54.5 + j17.2$ for muscle, $38.5 + j10$ for skin, $8 + j1$ for bone marrow, and $5.5 + j0.6$ for bones.

The GNI-CGLS algorithm converged after 24 iterations and the data misfit $\mathcal{F}^{\mathcal{LS}}$ at the last iteration was 4.7%. The inversion result using the GNI-CGLS algorithm is shown in Fig. 1(a) and (b), where the reconstruction results are very oscillatory. The MR enhancement procedure was then applied to this reconstruction which took 312 CG iterations applied to (5). The computation times were 31 min for the GNI-CGLS method and 4 min for the MR enhancement.

The enhanced reconstruction, shown in Fig. 1(c) and (d), shows the overall structure of the arm as well as the positions of the two bones clearly. It can easily be seen that the utilized MR suppresses the spurious oscillations in the original reconstruction and also preserve the edges of the two bones. The reconstructed permittivity for the muscle tissue is close to the expected value; however, the reconstructed permittivity of the bones is higher than the expected value. The difficulty in the reconstruction of the bone permittivity in this data set has also been reported in the multiplicative regularized contrast source inversion (MR-CSI) reconstruction of this target [22]. The MR-enhanced GNI-CGLS algorithm provides very similar results to the MR-CSI reconstruction for this data set [22].

The data misfit $\mathcal{F}^{\mathcal{LS}}$ for the enhanced reconstructed contrast is 5.2% which is slightly larger than the data misfit corresponding to the GNI-CGLS reconstructed contrast. This may
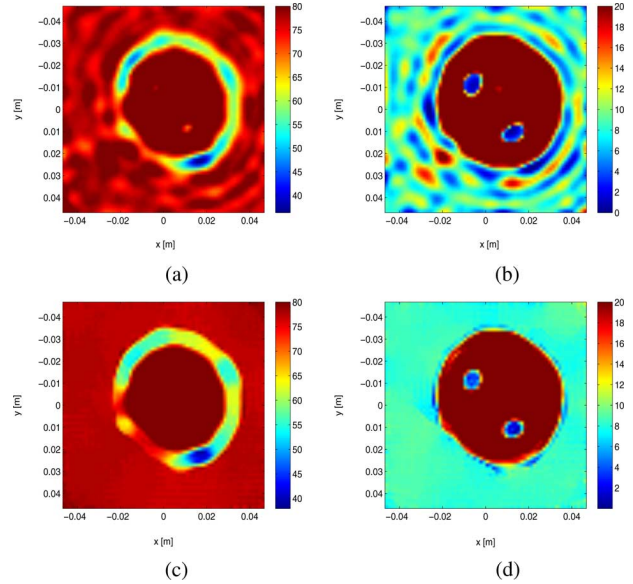
seem surprising at first, but it is well known that if inversion algorithms converge to where the data misfit is below the noise level, then the convergence is probably to the wrong local minimum. That is, a smaller data misfit cost-functional $\mathcal{F}^{\mathcal{LS}}$ does not necessarily mean a better reconstruction as the data misfit should not become smaller than the noise level of the calibrated measured data (Morozov discrepancy principle [23]). Due to several sources of error in the calibrated measured data such as modeling the horn antennas by line sources, possible temperature shifts and the actual measurement noise, it is not easy, if not impossible, to find the noise level of the calibrated measured data.

To show the performance of the MR enhancement when the GNI-CGLS algorithm is not completely converged, we consider the reconstructed contrast at the fifth iteration of the GNI-CGLS algorithm whose corresponding $\mathcal{F}^{\mathcal{LS}}$ is 20%. The reconstructed contrast at this iteration has been shown in Fig. 2(a) and (b). We now consider this contrast to be $\hat{\chi}$ in (4) and construct its corresponding linear operator $E_{\text{Lin}}^{\text{scat}}$. The MR enhancement was then performed which took 105 CG iterations. The enhanced contrast corresponding to this choice of $\hat{\chi}$ is shown in Fig. 2(c) and (d). It can be seen that the MR enhancement is also successful in enhancement of this contrast which is not the final converged solution of the GNI-CGLS method.

B. Institut Fresnel TE Data Set: FoamDielExtTE Target

This data set (data file: FoamDielExtTE.exp) is collected from a cylindrical target in free space for nine frequencies from 2 to 10 GHz, in 1 GHz step, by the Institut Fresnel, France in the TE mode [24]. The target is illuminated from eight views and the data is collected at 241 points per view. The measured TE data is then calibrated by a magnetic line source as in [25]. The target consists of a cylinder of diameter 31 mm with the relative permittivity $\epsilon_r = 3 \pm 0.3$ which is butted against another cylinder of diameter 80 mm with relative permittivity $\epsilon_r = 1.45 \pm 0.15$ as pictured in [24]. For this target,
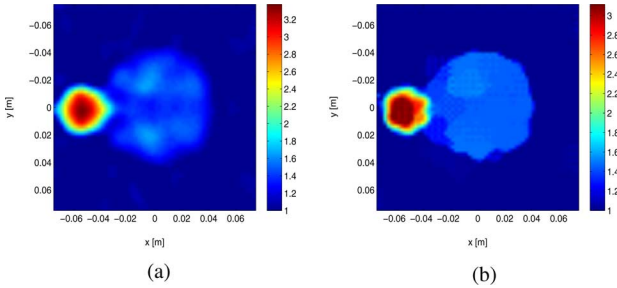
Fig. 3. Reconstruction of the *FoamDielExtTE* target (real part) (a) using the GNI-CGLS method and (b) using the MR-enhanced GNI-CGLS method. (a) $\text{Real}(\epsilon_r)$ and (b) $\text{Real}(\epsilon_r)$.

we consider the imaging domain $\mathcal{D}$ to be a 15 cm $\times$ 15 cm square discretized into 60×60 pulse basis functions. The GNI-CGLS inversion algorithm converged after 24 iterations where the real part of the reconstructed permittivity is shown in Fig. 3(a). The imaginary part of the reconstructed permittivity (not shown here) is very small indicating a lossless object. The data misfit $\mathcal{F}^{\mathcal{LS}}$ for the final reconstruction at 10 GHz is 4.3%. The MR enhancement of this reconstruction, which took 74 CG iterations applied to (5), is shown in Fig. 3(b). The computation times were 2 h and 57 min for the GNI-CGLS algorithm and 4 min for the MR enhancement. The data misfit for the enhanced reconstruction at 10 GHz is 4.1%. For this target, both reconstructions are very good due to having a high signal to noise ratio in the measured data as well as utilizing multiple-frequency data in the inversion. It should be noted that the MR-enhanced GNI-CGLS reconstruction is very similar the MR-CSI reconstruction of this target [25].

V. CONCLUSION

While adding little computational complexity to the inversion algorithm, the weighted L_2-norm total variation MR was successfully used to enhance the GNI-CGLS reconstruction results. The MR enhancement was useful in removing the oscillatory artifacts in the reconstructions considered herein. Whether such a post regularization procedure can be viewed as a general enhancement tool and for what type of artifacts or noise it will be an enhancement for, is left for future studies. Considering the fact that Krylov subspace schemes can provide a fast regularization method, this MR-enhanced GNI-CGLS method can be very appropriate for large-scale MWI problems.

APPENDIX
MULTIPLICATIVE REGULARIZED GAUSS–NEWTON INVERSION

The Gauss–Newton algorithm can also be applied to the multiplicatively regularized nonlinear cost-functional $\mathcal{F}^{\mathcal{LS}}(\chi)\mathcal{F}^{\mathcal{MR}}(\chi)$ [14], [18]. The Gauss-Newton correction at the nth stage of the GNI algorithm can then be found by solving

$$\left(\boldsymbol{J}_{n-1}^H \boldsymbol{J}_{n-1} + \frac{\mathcal{F}^{\mathcal{LS}}(\chi_{n-1})}{\mathcal{F}_n^{\mathcal{MR}}(\chi_{n-1})} \boldsymbol{\mathcal{L}}_n \right) \Delta\chi_n$$

$$= -\boldsymbol{J}_{n-1}^H \left(E_{n-1}^{\text{scat}} - E^{\text{meas}} \right) - \frac{\mathcal{F}^{\mathcal{LS}}(\chi_{n-1})}{\mathcal{F}_n^{\mathcal{MR}}(\chi_{n-1})} \boldsymbol{\mathcal{L}}_n \chi_n \quad (9)$$

where the operator $\boldsymbol{\mathcal{L}}_n$ represents the discrete form of $-\nabla \cdot (b_n \nabla)$ and the superscript H denotes the Hermitian operator.

We refer to this inversion algorithm as the multiplicative regularized Gauss–Newton inversion (MR-GNI) method.

Neglecting the computational complexity of applying $\boldsymbol{\mathcal{L}}_n$ to an arbitrary vector of the correct size, finding $\Delta\chi_n$ from (9) requires about $2P \times (2R_x T_x N)$ [26] where T_x denotes the number of transmitters, R_x the number of measurements per transmitter, N number of discretization in the imaging domain and P is the number of iterations required for the convergence of the CG algorithm applied to (9). Note that each iteration of the CG algorithm requires two matrix-vector multiplications. On the other hand, the GNI-CGLS scheme requires about $2k \times (R_x T_x N)$ operations to find $\Delta\chi_n$ when applied to (3) (k is the dimension of the projection). Assuming that the same forward solver and line search algorithm utilized in both the MR-GNI and GNI-CGLS methods, the ratio of the MR-GNI to GNI-CGLS computational cost is $2P/k$. As k is usually chosen to be a very small integer [1], the GNI-CGLS method is computationally more efficient than the MR-GNI method. Noting that the computational complexity of the MR enhancement procedure, as explained in Section III, is negligible compared to that of GNI-CGLS algorithm, the GNI-CGLS method with the MR enhancement is computationally more efficient than the MR-GNI method.

REFERENCES

[1] T. Rubæk, P. M. Meaney, P. Meincke, and K. D. Paulsen, "Nonlinear microwave imaging for breast-cancer screening using Gauss-Newton's method and the CGLS inversion algorithm," *IEEE Trans. Antennas Propag.*, vol. 55, no. 8, pp. 2320–2331, Aug. 2007.

[2] E. C. Fear, X. Li, S. C. Hagness, and M. Stuchly, "Confocal microwave imaging for breast cancer detection: Localization of tumors in three dimensions," *IEEE Trans. Biomed. Eng.*, vol. 49, no. 8, pp. 812–822, Aug. 2002.

[3] P. M. Meaney, T. Zhou, M. W. Fanning, S. A. Geimer, and K. D. Paulsen, "Microwave imaging for bone fracture risk assessment," in *Proc. 2008 Appl. Computational Electromagn. Symp.*, Niagra Falls, Canada, Mar. 31–Apr. 4 2008, pp. 462–466.

[4] S. Y. Semenov, R. H. Svenson, V. G. Posukh, A. G. Nazarov, Y. E. Sizov, A. E. Bulyshev, A. E. Souvorov, W. Chen, J. Kasell, and G. P. Tastis, "Dielectric spectroscopy of canine myocardium during acute ischemia and hypoxia at frequency spectrum from 100 KHz to 6 GHz," *IEEE Trans. Med. Imag*, vol. 21, no. 6, pp. 703–707, Jun. 2002.

[5] N. Joachimowicz, C. Pichot, and J. P. Hugonin, "Inverse scattering: An iterative numerical method for electromagnetic imaging," *IEEE Trans. Antennas Propag.*, vol. 39, no. 12, pp. 1742–1752, Dec. 1991.

[6] Q. Fang, P. Meaney, S. Geimer, A. Streltsov, and K. Paulsen, "Microwave image reconstruction from 3-D fields coupled to 2-D parameter estimation," *IEEE Trans. Med. Imag.*, vol. 23, no. 4, pp. 475–484, Apr. 2004.

[7] P. Meaney, K. Paulsen, B. Pogue, and M. Miga, "Microwave image reconstruction utilizing log-magnitude and unwrapped phase to improve high-contrast object recovery," *IEEE Trans. Med. Imag.*, vol. 20, no. 2, pp. 104–116, Feb. 2001.

[8] A. E. Bulyshev, A. E. Souvorov, S. Y. Semenov, R. H. Svenson, A. G. Nazarov, Y. E. Sizov, and G. P. Tastis, "Three dimensional microwave tomography. Theory and computer experiments in scalar approximation," *Inv. Probl.*, vol. 16, pp. 863–875, 2000.

[9] A. Bjork, *Numerical Methods for Least Squares Problems.*. Philadelphia, PA: SIAM, 1996.

[10] J. Chung, J. G. Nagy, and D. P. O'leary, "A weighted-GCV method for Lanczos-hybrid regularization," *Electron. Trans. Numer. Anal.*, vol. 28, pp. 149–167, 2008.

[11] P. Charbonnier, L. Blanc-Féraud, G. Aubert, and M. Barlaud, "Deterministic edge-preserving regularization in computed imaging," *IEEE Trans. Image Process.*, vol. 6, no. 2, pp. 298–311, Feb. 1997.

[12] J. D. Shea, P. Kosmas, S. C. Hagness, and B. D. van Veen, "Three dimensional microwave breast imaging: A bounded, multi-frequency inverse scattering solution on a uniform voxel mesh," presented at the XXIX General Assembly Int. Union Radio Sci., Chicago, IL, Aug. 2008.

[13] A. Abubakar, P. M. van den Berg, T. M. Habashy, and H. Braunisch, "A multiplicative regularization approach for deblurring problems," *IEEE Trans. Image Process.*, vol. 13, no. 11, pp. 1524–1532, Nov. 2004.

[14] A. Abubakar, T. M. Habashy, V. L. Druskin, L. Knizhnerman, and D. Alumbaugh, "2.5D forward and inverse modeling for interpreting low-frequency electromagnetic measurements," *Geophys.*, vol. 73, no. 4, pp. F165–F177, Jul.–Aug. 2008.

[15] T. M. Habashy and A. Abubakar, "A general framework for constraint minimization for the inversion of electromagnetic measurements," *Progr. Electromagn. Res.*, vol. 46, pp. 265–312, 2004.

[16] P. Lobel, C. Pichot, L. Blank-Féraud, and M. Barlaud, "Conjugate-gradient algorithm with edge-preserving regularization for image reconstruction from Ipswich data for mystery objects," *IEEE Antennas Propag. Mag.*, vol. 39, no. 2, pp. 12–14, Apr. 1997.

[17] C. Vogel and M. Oman, "Fast, robust total variation-based reconstruction of noisy, blurred images," *IEEE Trans. Image Process.*, vol. 7, no. 6, pp. 813–824, Jun. 1998.

[18] P. Mojabi and J. LoVetri, "Microwave biomedical imaging using the multiplicative regularized Gauss-Newton inversion," *IEEE Antennas Wireless Propag. Lett.*, vol. 8, pp. 645–648, 2009.

[19] P. Zwamborn and P. van den Berg, "The three dimensional weak form of the conjugate gradient FFT method for solving scattering problems," *IEEE Trans. Microwave Theory Tech.*, vol. 40, no. 9, pp. 1757–1766, Sep. 1992.

[20] A. G. Tijhuis, K. Belkebir, and A. C. S. Litman, "Theoretical and computational aspects of 2-D inverse profiling," *IEEE Trans. Geosci. Remote Sens.*, vol. 39, no. 6, pp. 1316–1330, Jun. 2001.

[21] A. Broquetas, J. Romeu, J. M. Rius, A. R. ElliasFuste, A. Cardama, and L. Jofre, "Cylindrical geometry: A further step in active microwave tomography," *IEEE Trans. Microwave Theory Tech.*, vol. 39, no. 5, pp. 836–844, May 1991.

[22] A. Abubakar, P. M. van den Berg, and J. J. Mallorqui, "Imaging of biomedical data using a multiplicative regularized contrast source inversion method," *IEEE Trans. Microwave Theory Tech.*, vol. 50, no. 7, pp. 1761–1777, Jul. 2002.

[23] C. Morozov, "On the solution of functional equations by the method of regularization," *Soviet Math. Dokl.*, vol. 7, pp. 414–417, 1966.

[24] J.-M. Geffrin, P. Sabouroux, and C. Eyraud, "Free space experimental scattering database continuation: Experimental set-up and measurement precision," *Inv. Probl.*, vol. 21, pp. S117–S130, 2005.

[25] A. Abubakar, P. M. van den Berg, and T. M. Habashy, "Application of the multiplicative regularized contrast source inversion method on TM and TE-polarized experimental fresnel data," *Inv. Probl.*, vol. 21, pp. S5–S13, 2005.

[26] P. Mojabi and J. LoVetri, "Overview and classification of some regularization techniques for the Gauss-Newton inversion method applied to inverse scattering problems," *IEEE Trans. Antennas Propag.*, vol. 57, no. 9, pp. 2658–2665, Sep. 2009.